Forces and symmetries in cells and tissues

Eckert, J.

Citation

Eckert, J. (2022, December 6). *Forces and symmetries in cells and tissues*. *Casimir PhD Series*. Retrieved from https://hdl.handle.net/1887/3492626

Chapter 4

Epithelia are multiscale active liquid crystals

Biological processes, such as embryogenesis, wound healing and cancer progression, crucially rely on the ability of epithelial cells to coordinate their mechanical activity over length scales larger than the typical cellular size. While regulated by various signaling pathways, it has recently become evident that this behavior can additionally hinge on a minimal toolkit of physical mechanisms, of which liquid crystal order is the most prominent example. Yet, experimental and theoretical studies have given so far inconsistent results in this respect: whereas *nematic* order is often invoked in the interpretation of experimental data, computational models have instead suggested that *hexatic* order could in fact serve as a linchpin for collective migration in confluent cell layers. In this article, we resolve this dilemma. Using a combination of *in vitro* experiments on Madin-Darby canine kidney cells (MDCK), numerical simulations and analytical work, we demonstrate that both nematic and hexatic order are in fact present in epithelial layers, with the former being dominant at large length scales and the latter at small length scales. In MDCK GII cells on uncoated glass, these different types of liquid crystal order crossover at 34 µm, corresponding approximately to clusters of 21 cells. Our work sheds light on the emergent organization of living matter, provides a new framework for deciphering the emergent organization of epithelia and paves the way toward a comprehensive and predictive mesoscopic theory of tissues.

This chapter is based on: Armengol-Collado, J.-M., Carenza, L. N., **Eckert, J.**, Krommydas, D., and Giomi, L. (2022). Epithelia are multiscale active liquid crystals. *arXiv:2202.00668, under revision.*

4.1 Introduction and results

An increasingly large body of evidence suggests that liquid crystal order could lie at the heart of a myriad of cellular processes that are instrumental for life (*1–7*). These include the extrusion of apoptotic cells (*2*), the development of sharp morphological features in developing embryos (*8*, *9*) or the onset of organism-wide cellular flows during morphogenesis (*10*). In confluent epithelial layers, detecting liquid crystal order is commonly achieved by tracking the longitudinal direction of individual cells by diagonalizing a rank−2 tensor − i.e. the so-called structure tensor (*11*) or equivalently the shape tensor (*12*, *13*) in case of segmented images − that embodies the geometry of the polygonal cells (Fig.4.1A). The resulting two-dimensional orientation field is then used to identify topological defects (*1–4*), which in turn provide a fingerprint of the underlying orientational order. Liquid crystal defects (also known as disclinations) are isolated singularities in the orientational field and can be classified according to their winding number or 'strength', s, defined as the number of revolutions of the orientation field along an arbitrary contour encircling the defect core (*14*). Because in a two-dimensional liquid crystal with p−fold rotational symmetry (i.e. symmetry under rotations by $2\pi/p$) this number must be an integer multiple of $1/p$, defects such as vortices, asters and spirals, for which $s = 1$, are a signature of a polar phase (i.e. $p = 1$); comet- and star-shaped disclinations, whose winding numbers are $s = 1/2$ and $s = -1/2$ respectively, are representative of a nematic phase (i.e. $p = 2$); whereas 5−fold and 7−fold disclinations, with $s = 1/6$ and $s = -1/6$, are the elementary topological defects in hexatics (i.e. $p = 6$).

Although inferring order from defects represents a consolidated strategy in liquid crystals science since the times of Georges Friedel (*15*) − who used it to decipher and classify phases such as nematic, cholesteric, and smectic − this specific protocol, based on tracking the cells' longitudinal direction, becomes progressively less reliable as p increases. To illustrate this issue, we show in Fig.4.1B how applying the same protocol to a perfect honeycomb lattice can lead to the misdetection of a pair of $\pm 1/2$ nematic disclinations. This originates from the fact that, while regular hexagons are invariant under rotations by 60°, the orientation field constructed from the longitudinal direction of hexagonal cells cannot discriminate between the three equivalent directions defined by pairs of opposite vertices. Similarly, in Fig.4.1C and Fig.4.1D we show how detecting an elementary hexatic disclination correctly yields a topological defect, but with incorrect winding number $s = 1$.

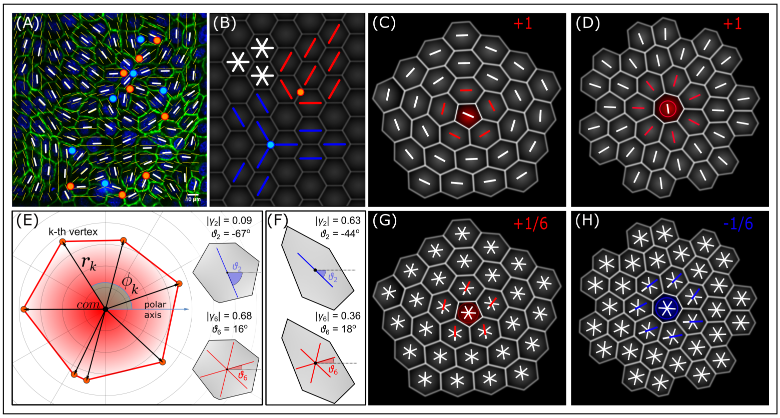

Figure 4.1: Topological defects and** $p-$**fold rotational symmetry. *(**A**), A typical configuration of the nematic orientation field (white rods), obtained from a sample of MDCK GII cells upon diagonalizing the shape tensor (12, 13). Yellow rods represent the interpolated nematic field. Here and in the following, positive and negative defects are marked in red and blue, respectively, regardless of the magnitude of their winding number. (**B**), Because of the* $6-$*fold symmetry of regular hexagons, there is no well-defined longitudinal direction, thus it is possible to construct a defective configuration, featuring a pair of* $\pm 1/2$ *disclinations, even though the lattice is defect free. (**C,D**), Disclinations in hexatics consist of pentagonal (i.e.* $s = 1/6$*) and heptagonal (i.e.* $s = -1/6$*) sites embedded in an otherwise* $6-$*fold background. Attempting to detect these elementary defects by tracking the longitudinal direction of the cells (with rods), correctly yields a defect at the center of the clusters, however, because of the mismatch between the* $6-$*fold symmetry of the configuration and the* $2-$*fold symmetry of the order parameter both defects are detected with the incorrect winding number* $s = 1$*. (**E**), Graphical representation of the* $p-$*fold order parameter, Eq.(4.2), for a generic polygon (heptagon). The quantities* $\boldsymbol{r}_k = \{x_k, y_k\}$ *and* $\phi_k = \arctan(y_k/x_k)$ *represent, respectively, the position of the vertices of the polygon with respect to its center of mass (i.e. com) and their orientation with respect to the horizontal direction (i.e. polar axis). The inset shows the nematic (top) and hexatic (bottom) order parameter,* γ_p*, superimposed on the polygonal shape of the main panel. (**F**), Example of the* γ_p *order parameter, Eq.(4.2), for an elongated hexagon. The irregular heptagon in panel (**E**) is closer in shape to a regular hexagon, thus the order parameter* γ_6 *is an order of magnitude larger than* γ_2*. The outcome is reversed in the irregular hexagon in panel (**F**), which, as a consequence of its elongation and despite being* $6-$*sided, yields* $\gamma_2 > \gamma_6$*. In both panels, the blue rods and the* $6-$*legged stars correspond respectively to the* $2-$*fold and* $6-$*fold orientations of the polygons and are oriented in such a way that maximizes the overall probability of finding a vertex in the direction of the legs. (**H,I**), The correct recognition of the hexatic disclinations are shown in panels (**C**) and (**D**) using* γ_6*. In both panels, one of the legs of the order parameter has been colored as a guide to the eye. By following the order parameter along a positive oriented (anticlockwise) close loop encircling the defect core, the red leg rotates anticlockwise for the positive defect in panel (**E**). After a full rotation, the colored leg rotates of an angle* $2\pi/6$ *corresponding to a winding number* $s = 1/6$*. Conversely, in panel (**I**) the blue leg rotates clockwise and covers an angular displacement of* $-\pi/3$ *corresponding to a winding number* $s = -1/6$*.*

To overcome this difficulty, here we introduce a generalized rank$-p$ shape tensor, able to capture arbitrary $p-$fold rotational symmetries, with p any natural number. Given the polygonal contour of a cell, whose V vertices have coordinates $\boldsymbol{r}_k = \{x_k, y_k\}$ with respect to the cell's center of mass (Fig.4.1E), our generalized shape tensor can be defined as

$$\boldsymbol{G}_p = \frac{1}{\Delta_p} \left[\!\!\left[\sum_{k=1}^{V} \underbrace{\boldsymbol{r}_k \otimes \boldsymbol{r}_k \otimes \cdots \otimes \boldsymbol{r}_k}_{p\,\text{times}} \right]\!\!\right] , \tag{4.1}$$

where $\Delta_p = \sum_{k=1}^{V} |\boldsymbol{r}_k|^p$, and the operator $[\![\cdots]\!]$ has the effect of rendering its argument symmetric and traceless. For tensors whose rank is higher than two, the property of being traceless implies that contracting any two indices of the tensor yields zero. For $p = 2$, Eq.(4.1) gives, up to a normalization constant, the traceless part of the standard rank-2 shape tensor (*12*, *13*). Regardless of its rank, the tensor $\boldsymbol{G}_p$ has only two linearly independent components in two dimensions (*16*, *17*), from which one can extract information about the cells' orientation and anisotropy. In particular, using a generalization of the spectral theorem to tensors with arbitrary rank (*18*), one can show that all elements of $\boldsymbol{G}_p$ are proportional to either the real or the imaginary part of the complex order parameter

$$\gamma_p = \frac{1}{\Delta_p} \sum_{k=1}^{V} |\boldsymbol{r}_k|^p e^{ip\phi_k} = |\gamma_p| e^{ip\vartheta_p}, \tag{4.2}$$

where $\phi_k = \arctan(y_k/x_k)$ the angular coordinate of the $k-$th vertex of a given cell (Fig.4.1E). The angle ϑ_p, on the other hand, corresponds to the $p-$fold orientation of the whole cell with respect to the horizontal direction. In practice, this is equivalent to the inclination of a $p-$legged star centered at the cell's center of mass and oriented in such a way to maximize the probability of finding a vertex in the direction of either one of the legs. Some examples of this construction are shown in Fig.4.1E and Fig.4.1F, where γ_p is computed for more or less elongated irregular polygons. When applied to defective configurations, our method yields the correct winding numbers $s = \pm 1/6$ (Fig.4.1G and Fig.4.1H).

With the tensor $\boldsymbol{G}_p$ in hand, we next investigate the emergent orientational order in confluent monolayers of MDCK GII cells (Fig.4.2A and Fig.4.2B). After segmenting the images by taking advantage of the previous labeling of E-cadherin, we track the cells' contour and from the coordinates of the vertices we compute the order parameter γ_p, Eq.(4.2). We analyze a total of 68 images of confluent monolayers (see the Methods for details) with each one of them comprising 140 ± 31 cells (mean ± s.d.). Fig.4.2C shows the probability distribution of γ_p for $p = 2$ and $p = 6$. Interestingly, the distribution of γ_6 is symmetric and spreads over a broad range of values; conversely, the distribution of γ_2 features a peak at approximately 0.35, with a decreasing tail at larger values. The MDCK GII cells analyzed in this study are, therefore, more prone to arrange in isotropic rather than elongated shapes.

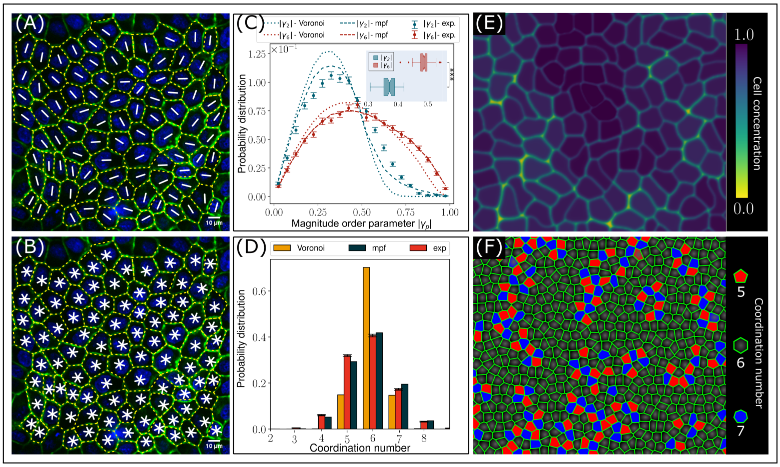

Figure 4.2: Symmetry of MDCK cells in confluent monolayers. *(**A**,**B**), Confocal image of a confluent MDCK GII monolayer (green, E-cadherin and blue, nuclei). The dashed yellow lines trace the contour of the cells as identified after image segmentation. The white rods (**A**) and stars (**B**) respectively mark the 2−fold and 6−fold orientation of cells and have been obtained from the order parameter γ_p, Eq.(4.2). (**C**), Probability distribution of the magnitude of the order parameter $|\gamma_p|$ for $p = 2$ (blue) and $p = 6$ (red). Experimental data points are obtained by averaging over 68 different images, with each containing 140 ± 31 (mean ± s.d.) cells. The mean value of the distributions are $\langle|\gamma_2|\rangle = 0.370 \pm 0.030$ (mean ± s.d.) and $\langle|\gamma_6|\rangle = 0.49 \pm 0.05$ (mean ± s.d.). The boxplot in the inset shows the average magnitudes of the order parameters of 68 imaged monolayers. $\langle|\gamma_2|\rangle$ and $\langle|\gamma_6|\rangle$ are significantly different with a p-value < 0.0001, calculated by using the two-sided Wilcoxon rank sum test. Dashed and dotted lines are obtained from numerical simulations of the multiphase-field (mpf) and Voronoi models. (**D**), Probability distribution of cell coordination number for experiments and simulations. The height of the bar represents the mean of 68 analyzed images. The mean values of the coordination number distributions are 5.8 ± 0.9 (mean ± s.d.) for experiments, 5.9 ± 0.9 (mean ± s.d.) for multiphase field simulations, and 6.0 ± 0.6 (mean ± s.d.) for Voronoi simulations. In (**C**) and (**D**), error bars are computed from the standard error of mean. (**E**), Contour plot of the local cell concentration of a multiphase-field simulation with 360 cells in a magnified region of the simulation box, showing approximately one third of the system. Darker regions correspond to areas dense with cells and lighter regions to areas where cells are sparser (see legend box). (**F**), Configuration of a numerical simulation of the Voronoi model. The cells in red (blue) have 5 (7) neighbors, while others have 6.*

This results in a disordered and yet orientationally coherent tiling of the plane, where a majority of hexagons coexists with large minorities of pentagons and heptagons, as indicated by the distribution of the number of neighbors in Fig.4.2D. We compare these observations with numerical simulations of two different theoretical models of epithelia: i.e. a continuous multiphase field model (mpf) (Fig.4.2E; (*19–21*)) and the discrete Voronoi model (Fig.4.2F; (*22*)), both in qualitative agreement with experimental data.

In order to quantify the amount of orientational order in the system, we next compare the orientation of each cell with that of its neighbors, by means of the following coarse-graining procedure. Given a disk $\Omega_R = \Omega_R(\boldsymbol{r})$, with radius R and centered at $\boldsymbol{r}$, and letting $\boldsymbol{r}_c$ be the position of the center of mass of the $c-$th cell, we define the coarse-grained order field $\Gamma_p = \Gamma_p(\boldsymbol{r})$ as

$$\Gamma_p = \frac{1}{N} \sum_{c=1}^{N} \gamma_p(\boldsymbol{r}_c) = |\Gamma_p| e^{ip\theta_p}, \tag{4.3}$$

where N is the number of cells whose center of mass lies within Ω_R, while $|\Gamma_p| = |\Gamma_p(\boldsymbol{r})|$ and $\theta_p = \theta_p(\boldsymbol{r})$ are respectively the magnitude and phase of the complex order parameter Γ_p, conveying information about the amount and direction of $p-$fold orientational order at the length scale R (Fig.4.3A).

The outcome of this analysis is shown in Fig.4.3B and Fig.4.3C. At length scales comparable with the average cell size – i.e. $R \lesssim R_{\text{cell}}$, with $R_{\text{cell}}= 7.4 \pm 1.9$ μm the average cell radius computed as half of the distance between the cells' centers of mass – both the nematic (Fig.4.3B) and the hexatic (Fig.4.3C) coarse-grained fields are populated by topological defects. For $p = 6$, in particular, the monolayer appears organized into regions characterized by spatially uniform hexatic order, separated by arrays of $\pm 1/6$ disclinations, similarly to grains and grain boundaries in polycrystals (*23*). Increasing R has the effect of smoothing the Γ_6 field, thereby absorbing neutral pairs of disclinations into a gently varying $6-$fold orientation field, resulting in a power law decreasing defect density (Fig.4.3D).

The scenario differs dramatically for $p = 2$ (Fig.4.3B). In this case, many of the defective structures identified in the configuration of the hexatic field at the small length scales are replaced by very sharp and yet defect-free textures. This peculiarity originates precisely from the mismatch between the actual $6-$fold symmetry of the configuration at the cellular scale and the $2-$fold symmetry of the order parameter used to describe it, in a similar fashion as using a (polar) vector field to describe a nematic disclination gives rise to singular lines where the polar field 'jumps' by an angle π (Fig.4.3E).

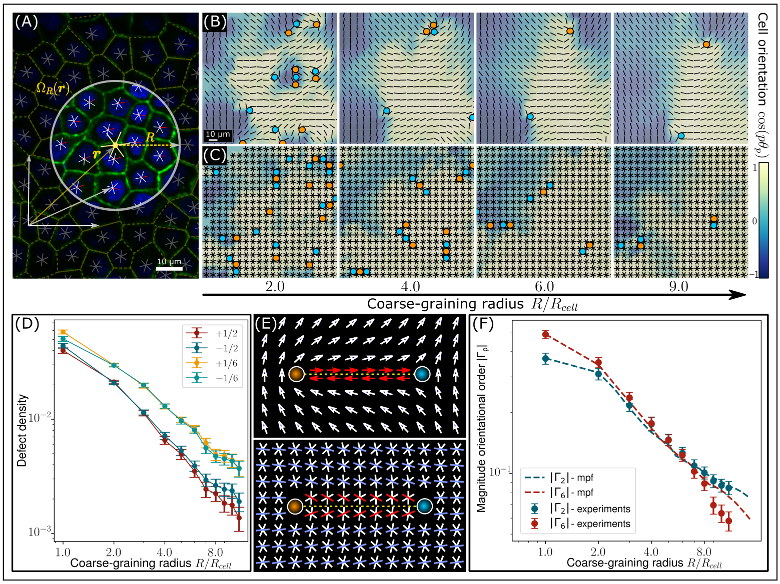

Figure 4.3: Coarse-graining and multiscale features of confluent cell monolayers. *(**A**), Illustration of the coarse-graining procedure entailed in Eq.(4.3). A disk* $\Omega_R = \Omega_R(\boldsymbol{r})$ *(encircled in gray), with radius* R *and centered at the point* $\boldsymbol{r}$ *(in general not coincident with the center of mass of any specific cell) is superimposed to a segmented image of the cell monolayer and the cells in its interior are used to compute the coarse-grained filed* Γ_p*. The large yellow star at the center of the disk shows the orientation of the whole cluster. (**B,C**), Nematic (top row) and hexatic (bottom row) coarse-grained fields* Γ_2 *and* Γ_6 *versus the coarse-graining radius* R*, expressed in units of the average cell size* $R_{\text{cell}} = 7.4\,\mu m$*. In both panels, positive and negative defects are marked in red and blue, respectively (*$\pm 1/2$ *for nematic and* $\pm 1/6$ *for hexatic). (**D**), Defect density at varying the coarse-graining radius* R*. (**E**), A mismatch between the defect charge and the symmetry of the* $p-$*atic liquid crystal gives rise to unphysical singular line (see Sec. S4.4.2). Top (bottom) panel shows a pair of nematic (hexatic) defects of winding number* $s = \pm 1/2$ *(*$s = \pm 1/6$*). (**F**), Magnitude of* Γ_2 *and* Γ_6 *versus the coarse-graining radius* R *measured from experimental and numerical mpf data. Both data sets fit the power law* $|\Gamma_p| = \langle \gamma_p \rangle (R/R_{\text{cell}})^{-\eta_p/2}$*, with* η_p *a non-universal exponent (16, 17), with the following fitting parameters: (experiments)* $\eta_2 = 0.41 \pm 0.01$*,* $\eta_6 = 0.49 \pm 0.01$*; (mpf)* $\eta_2 = 0.43 \pm 0.02$*,* $\eta_6 = 0.48 \pm 0.01$*. In both experiments and multiphase field simulations, the* $|\Gamma_2|$ *and* $|\Gamma_6|$ *order parameters crossover at the length scale* $R_\times$*, with: (experiment)* $R_\times / R_{\text{cell}} = 4.6 \pm 1.0$*; (mpf)* $R_\times / R_{\text{cell}} = 5.0 \pm 1.2$*. In (**D**) and (**F**), the error bars correspond to the standard error of the mean.*

Conversely, at larger length scales, the majority of nematic defects is replaced by regions where the nematic field Γ_2 smoothly varies across the sample, with exception for a small number of isolated $\pm 1/2$ disclinations (Fig.4.3B and Fig.4.3D). These observations are further supported by the scaling behavior of the magnitude of the fields Γ_2 and Γ_6 as the coarse-graining radius R varies (Fig.4.3F). In particular, both $|\Gamma_2|$ and $|\Gamma_6|$ are finite at all length scales in the range $1 \leq R/R_{\rm cell} < 10$, but, while $|\Gamma_6|$ is prominent at small length scales, this is overweighted by $|\Gamma_2|$ at large length scales. For our MDCK GII cells on uncoated glass, the crossover occurs at $R_\times/R_{\rm cell} = 4.6 \pm 1.0$, corresponding to clusters of approximately 21 cells. The same crossover is also observed in our numerical simulations of the multiphase field model, with the crossover scale $R_\times/R_{\rm cell} = 5.0 \pm 1.2$, while it is not found in simulations of the Voronoi model, where hexatic order is dominant at all length scales.

Taken together, our experimental and numerical results demonstrate that epithelial monolayers behave as multiscale active liquid crystals, with 6−fold hexatic order characterizing the spatial organization of the cells at small length scales, while nematic order dictates the large-scale structure of the monolayer. The crossover length scale is, as intuitive, non-universal, but depends on the molecular repertoire and the material properties of the specific phenotype, as well as on the mechanical properties and the surface chemistry of the substrate.

4.2 Discussion and conclusion

In conclusion, we have investigated the multiscale physics of epithelial layers, finding that multiple types of liquid crystal order can coexist at different length scales. In particular, hexatic order is prominent at the cellular scale (i.e. in clusters of up to 21 cells in our MDCK GII samples) while nematic order characterizes the structure of the monolayer at larger length scales. This hierarchical structure is expected to complement the complex network of regulatory pathways that tissues have at their disposal (*24*) to coordinate the activity of individual cells to achieve multicellular organization (*25*). The novel approach introduced here creates the basis for a correct identification of topological defects – whose biophysical role in epithelia has recently focused great attention (*1–3*), especially in the context of morphogenesis (*8*, *10*, *26*, *27*) – and further provides the necessary knowledge for the foundation of a comprehensive and predictive mesoscopic theory of collective cell migration (*28*). In addition, our findings highlight a number of potentially crucial properties of epithelial tissues. First, collective cell migration in epithelia relies on both remodeling events at the small scale – such as cell intercalation and the rearrangement of multicellular rosettes (*29*, *30*) – as well as large scale flows (*10*). Therefore, the underlying *hexanematic* multiscale organization and the specific magnitude of the crossover scale $R_\times$ are expected to have a profound impact on how the geometry of the environment affects the specific migration strategy. E.g. metastatic cells traveling through micron-sized channels in the extracellular matrix during cancer invasion (*31*) will more likely rely on local hexatic-controlled remodeling events, whereas unconfined wound healing processes (*32*) are more likely to leverage on system-wide nematic-driven collective flows. Second, as both hexatic and nematic liquid crystals can feature topological defects, these are expected to interact, thereby affecting processes such as the extrusion of apoptotic cells (*2*), the development of sharp features during morphogenesis (*8*, *9*) and, in general, any remodeling or morphogenetic event that can take advantage of the persistent pressure variations introduced by active defects (*3*). Finally, in the light of what said above, it is evident that understanding how the crossover scale $R_\times$ can be controlled, either chemically or mechanically, may ultimately represent the key toward deciphering tissues' collective dynamics.

4.3 Materials and methods

Cell culture

Parental Madin-Darby Canine Kidney (MDCK) GII cells stably expressing E-cadherin-GFP (*33*) (kindly provided by M. Gloerich, UMC Utrecht) were cultured in a 1:1 ratio of low glucose DMEM (D6046; Sigma-Aldrich, St. Louis, MO) and Nutrient Mixture F-12 Ham (N4888; Sigma-Aldrich, St. Louis, MO) supplemented with 10% fetal calf serum (Thermo Fisher Scientific, Waltham, MA), and 100 mg/mL penicillin/streptomycin, 37 °C, 5% CO_2. For experiments, cells were seeded on uncoated cover glasses, grew to confluence, and nuclei were live-stained with 2 µg/mL Hoechst 34580 (Thermo Fisher, H21486) before imaging.

Microscopy

Samples were imaged at high resolution on a home-build optical microscope setup based on an inverted Axiovert200 microscope body (Zeiss), a spinning disk unit (CSU-X1, Yokogawa), and an emCCD camera (iXon 897, Andor). IQ-software (Andor) was used for setup-control and data acquisition. Illumination was performed using fiber-coupling of different lasers (405 nm (CrystalLaser) and 488 nm (Coherent)). Cells on over glasses were inspected with an EC Plan-NEOFLUAR 40× 1.3 Oil immersion objective (Zeiss). Images were taken in three focal-planes within a distance of 352 nm for a maximal intensity projection.

Analysis

Shape order parameter. Cell boundaries of confluent monolayers were analyzed using a maximum intensity projection of $z-$stack images. Cell segmentation and vertex analysis were performed using home-build Matlab scripts (Mathworks, Matlab R2018a). The number of nearest neighbors corresponds to the number of vertices surrounding a cell. The centroid of the polygon was calculated by $\boldsymbol{r}_c = \sum_{i=1}^{V} \boldsymbol{r}_i/V$, where V is the number of vertices and $\boldsymbol{r}_i$ their positions. For each cell, the shape order was derived by using Eq.(4.2). On average, we analyzed 140 ± 31 cells per image. For the probability distribution of the shape order for each analyzed image, we choose a binning of 20 ranging from 0 to 1.

Coarse-graining. The radius used to construct the coarse-grained field, given by Eq.(4.3), was chosen according to the typical cell radius $R_{\text{cell}} = 7.4 \pm 1.9\,\mu\text{m}$, calculated as half of the average cell-cell nearest neighbor distance. For calculating the crossover point, we set the center point of the disk equal to the center point of the image. The radius of the disk in which the complex order parameters were averaged ranged from R_{cell} to half of the image size ($176 \times 176\,\mu\text{m}$). For computing the nematic and hexatic coarse-grained director field, we set the grid-distance to R_{cell}.

Topological defects. Topological defects were identified by first interpolating the $p-$fold orientation field on a square 22×22 grid by means of the coarse-graining procedure in Eq.(4.3) and then computing the winding number along each unit cell. That is:

$$s = \frac{1}{2\pi} \oint_{\Box} \mathrm{d}\theta_p = \frac{1}{2\pi} \sum_{n=1}^{4} \left[\theta_p(\boldsymbol{r}_{n+1}) - \theta_p(\boldsymbol{r}_n)\right] \bmod \frac{2\pi}{p}, \tag{4.4}$$

where the symbol $\Box$ denotes a square unit cell in the interpolation grid and the mod operator constraints the difference $\theta_p(\boldsymbol{r}_{n+1}) - \theta_p(\boldsymbol{r}_n)$ in the interval $[-\pi/p, \pi/p]$.

Statistics

In total, 68 images of confluent monolayers (nine coverslips, three independent experiments) were taken and analyzed. In total, 9496 cells were considered for the analysis.

Numerical simulations

We make use of two different numerical models for ET previously introduced in literature: *(i)* the multiphase field model and *(ii)* the Voronoi model.

Multiphase field model. This model has been used to study the dynamics of confluent cell monolayers (*19*) and the mechanics of cell extrusion (*20*). It is a continuous model where each cell is described by a concentration field $\varphi_c = \varphi_c(\boldsymbol{r})$, with $c = 1, 2 \ldots N_{\text{cell}}$ and N_{cell} the total number of cells. The equilibrium state is defined by the free energy $\mathcal{F} = \int \mathrm{d}A\, f$ where the free energy density f is given by

$$
\begin{aligned}
f = \frac{\alpha}{4} \sum_c \varphi_c^2 (\varphi_c - \varphi_0)^2 + \frac{k_\varphi}{2} \sum_c (\nabla \varphi_c)^2 \\
+ \epsilon \sum_{c<c'} \varphi_c^2 \varphi_{c'}^2 + \sum_c \lambda \left(1 - \frac{1}{\pi \varphi_0^2 R_\varphi^2} \int \mathrm{d}A\, \varphi_c^2 \right)^2 . \qquad (4.5)
\end{aligned}
$$

Here, α and k_φ are material parameters which can be used to tune the surface tension $\gamma = \sqrt{8\kappa_\varphi \alpha}$ and the interfacial thickness $\xi = \sqrt{2\kappa_\varphi/\alpha}$ of isolated cells and thermodynamically favor spherical cell shapes. The constant ϵ captures the repulsion between cells. The concentration field is large (i.e. $\varphi_i \simeq \varphi_0$) inside the cells and zero outside. The contribution proportional to λ in the free energy enforces cell incompressibility whose nominal radius is given by R_φ. The phase field φ_i evolves according to the Allen-Cahn equation

$$
\partial_t \varphi_c + \boldsymbol{v}_c \cdot \nabla \varphi_c = -M \, \frac{\delta \mathcal{F}}{\delta \phi_c} , \qquad (4.6)
$$

where $\boldsymbol{v}_i = v_0(\cos\theta_c \, \boldsymbol{e}_x + \sin\theta_c \, \boldsymbol{e}_y)$ is the velocity at which the $c-$th cell self-propels, with v_0 a constant speed and θ_c an angle. The latter evolves according to the stochastic equation

$$
\frac{\mathrm{d}\theta_c}{\mathrm{d}t} = \sqrt{2D}\, W_c , \qquad (4.7)
$$

where D is a constant controlling noise diffusivity and $W_c = W_c(t)$ is a Wiener process. The constant M in Eq.(4.6) is the mobility, measuring the relevance of thermodynamic relaxation with respect to non-equilibrium cell migration. Eq.(4.6) is solved with a finite-difference approach through a predictor-corrector finite difference Euler scheme implementing second order stencil for space derivatives (*21*). Simulation details and scaling to physical units are given in Tab.4.1.

Voronoi model. This model portrays a confluent tissue as a Voronoi tessellation of the plane (*22*). Each cell is characterized by two dynamical variables: the position $\boldsymbol{r}_c$ and the velocity $\boldsymbol{v}_c = v_0(\cos\theta_c\,\boldsymbol{e}_x + \sin\theta_c\,\boldsymbol{e}_y)$ with v_0 a constant speed and θ_c an angle, with $c = 1, 2 \dots N_{\text{cell}}$ and N_{cell} the total number of cells. The dynamics of these variables is governed by the following set of ordinary differential equations

$$\frac{\mathrm{d}\boldsymbol{r}_c}{\mathrm{d}t} = \boldsymbol{v}_c - \mu\nabla_{\boldsymbol{r}_c}E, \tag{4.8a}$$

$$\frac{\mathrm{d}\theta_c}{\mathrm{d}t} = \eta_c, \tag{4.8b}$$

where μ is a mobility coefficient and $E = E(\boldsymbol{r}_1, \boldsymbol{r}_2 \dots \boldsymbol{r}_{N_{\text{cell}}})$ is an energy function defined as

$$E = \sum_c \left[K_A\left(A_c - A_0\right)^2 + K_P\left(P_c - P_0\right)^2\right]. \tag{4.9}$$

Here, A_c and P_c are respectively the area and perimeter of each cell and A_0 and P_0 their preferred values. The variable η_c in Eq.(4.8b) is white noise, having zero mean and correlation function

$$\langle\eta_c(t)\eta_{c'}(t')\rangle = 2D_{\mathrm{r}}\delta_{cc'}\delta(t - t')\ , \tag{4.10}$$

with D_{r} a rotational diffusion coefficient. Simulation details and scaling to physical units are given in Tab.4.1.

Numerical model				
Multiphase field model				
Model parameter		Dimension	Simulation value(s)	Physical scaling
Lattice parameters	N_{cell}	—	361	—
	Δx	L	1	0.685 µm
	Δt	T	1	1.414 s
	L_x, L_y	L	380	246.6 µm
Free energy parameters	$M\alpha$	$1/T$	0.006	0.0042 s^{-1}
	Mk_φ	L^2/T	0.012	0.0040 $\mu\mathrm{m}^2\ \mathrm{s}^{-1}$
	$M\epsilon$	$1/T$	0.01	0.0071 s^{-1}
	$M\lambda$	$1/T$	600	$424,4\ \mathrm{s}^{-1}$
	φ_0	—	2.0	—
	R	L	10.86	7.4 µm
	$\xi = \sqrt{2k_\varphi/\alpha}$	L	2	1.37 µm
	$M\gamma = M\sqrt{8/9k_\varphi\alpha}$	L/T	0.008	0.0039 µm s^{-1}
Dynamical equation parameter	D_r^{pf}	$1/T$	0.0001	0.00007 s^{-1}
	v_0	L/T	0.0035	0.00169 µm s^{-1}
Dimensionless numbers	Peclét number $Pe = v_0/(D_r R)$	—	3.22	—
	Cell deformability $d = \epsilon/\alpha$	—	1.66	—
Voronoi model				
Lattice parameters	N_{cell}	—	22500	—
	Δt	T	0.01	0.53 s
	L_x, L_y	L	150	2220 µm
Energy parameters	μK_A	$1/(L^2T)$	1	0.0086 $\mu\mathrm{s}^{-1}$
	μK_P	$1/T$	1	0.98 s^{-1}
	A_0	L^2	1	219.04 $\mu\mathrm{m}^{-2}$
	P_0	L	3.9	57.72 µm
Dynamical equation parameter	v_0	L/T	0.1	27.8 µm s^{-1}
	D_r'	$1/T$	1	0.019 s^{-1}
Dimensionless numbers	Peclét $Pe = v_0/(D_r^V\sqrt{A_0})$	—	0.1	—
	Shape index $p_0 = P_0/\sqrt{A_0}$	—	3.9	—

Table 4.1: Physical scaling of simulation parameters. *The table provides the parameters used to perform simulations for both the multiphase field and the Voronoi model, together with their dimensions and scaling to physical units. For the multiphase field model, scaling is performed by equating the mean cell radius* R_{cell} *(*$\simeq$ *7.4* μm*) measured in experiments with the nominal cell radius* R *and a typical migration speed of cells in MDCK monolayers (4) (*$\simeq 2\ \mu m\ h^{-1}$*) with that measured in our simulations (*$\simeq 0.0011\ \Delta x/\Delta t$*). This allows us to find the physical scaling of the lattice grid unit* Δx *and the iteration unit* Δt*. For the Voronoi model, we equated the mean cell radius* R_{cell} *in experiments with that measured in simulations (*$\simeq$ *1). The time-step was derived with the same procedure as described for the multiphase field model. In the table, simulation values are given in both lattice and physical units, in columns four and five, respectively. Notice that we did not introduce an energy scale as this cancels out with the mobility parameter* M *in Eq.(4.6) and* μ *in Eq.(4.8), respectively.*

Acknowledgements

This work is supported by the European Union via the ERC-CoGgrant HexaTissue (L.N.C., D.K. and L.G.) and by Netherlands Organization for Scientific Research (NWO/OCW) as part of the research program 'The active matter physics of collective metastasis' with project number Science-

XL 2019.022 (J.-M.A.-C. and L.G.). Part of this work was carried out on the Dutch national e-infrastructure with the support of SURF through the Grant 2021.028 for computational time. J.E. and L.G. acknowledge M. Gloerich, UMC Utrecht, for providing us the MDCK cells. All authors acknowledge Ludwig Hoffmann for fruitful discussions.

Author contributions

J.-M.A.-C. performed analytic work, Voronoi model simulations and analyzed data. L.N.C. coordinated the research, performed the multiphase field simulations and analyzed data. J.E. performed analytic work, experiments and analyzed data. D.K. performed analytic work and analyzed data. L.G. devised and coordinated the research. All authors wrote the paper. J.-M.A.-C., L.N.C., J.E. and D.K. contributed equally to this work.

Author information

The authors declare no competing financial interests.

4.4 Supplementary

S4.4.1 The $p-$fold shape tensor

Definition and basic properties

In this supplementary Section, we explain the relation between the $p-$fold shape tensor $\boldsymbol{G}_p$, Eq.(4.1), and the complex order parameter γ_p, Eq.(4.2). To build up intuition, we start from observing that the standard rank-2 shape tensor for a $V-$sided polygon, is given by (*9*, *34*)

$$\boldsymbol{S} = \frac{1}{V} \sum_{k=1}^{V} \boldsymbol{r}_k \otimes \boldsymbol{r}_k \;, \tag{S4.11}$$

where, as in the main text, $\boldsymbol{r}_k$ represents the coordinate of the $k-$th vertex with respect to the center of mass of the cell. The spectral theorem allows one to represent $\boldsymbol{S}$, as well as any other symmetric tensor, in terms of two irreducible components, one diagonal and the other traceless:

$$\boldsymbol{S} = \bar{\lambda}\,\mathbb{1} + \Delta\lambda \left(\boldsymbol{e}_1 \otimes \boldsymbol{e}_1 - \frac{1}{2}\,\mathbb{1} \right) \;, \tag{S4.12}$$

where we have set

$$\bar{\lambda} = \frac{\lambda_1 + \lambda_2}{2} \;, \qquad \Delta\lambda = \lambda_1 - \lambda_2 \;,$$

with $\lambda_1 > \lambda_2$ the two eigenvalues of $\boldsymbol{S}$, $\boldsymbol{e}_1 = \cos\vartheta\,\boldsymbol{e}_x + \sin\vartheta\,\boldsymbol{e}_y$ the unit eigenvector associated with the largest eigenvalue λ_1 and $\mathbb{1}$ the rank-2 identity tensor. The two terms in Eq.(S4.12) entail information about the polygon's size and anisotropy. The latter property can be further highlighted by introducing the tensor

$$\boldsymbol{G}_2 = \frac{[\![\boldsymbol{S}]\!]}{\Delta_2} = \frac{\Delta\lambda}{\Delta_2}\,[\![\boldsymbol{e}_1^{\otimes 2}]\!] \;, \tag{S4.13}$$

where $\Delta_2 = \sum_{k=1}^{V} |\boldsymbol{r}_k|^2$, the operator $[\![\cdots]\!]$ has the effect of rendering its argument traceless and symmetric (*13*, *14*) and the $(\cdots)^{\otimes p}$ implies a $p-$fold tensorial product of the argument with itself: i.e.

$$\boldsymbol{e}_1^{\otimes p} = \underbrace{\boldsymbol{e}_1 \otimes \boldsymbol{e}_1 \otimes \cdots \otimes \boldsymbol{e}_1}_{p\,\text{times}} \;. \tag{S4.14}$$

In two dimensions, the tensor $\boldsymbol{G}_2$ has only two linearly independent components and expressing it in the basis $\{\boldsymbol{e}_x, \boldsymbol{e}_y\}$ readily gives

$$\boldsymbol{G}_2 = \frac{\Delta\lambda}{2\Delta_2}\begin{bmatrix} \cos 2\vartheta & \sin 2\vartheta \\ \sin 2\vartheta & -\cos 2\vartheta \end{bmatrix} \;. \tag{S4.15}$$

Furthermore, explicitly diagonalizing Eq.(S4.11) gives

$$\vartheta = \frac{1}{2}\,\arctan\left(\frac{\sum_{k=1}^{V} |\boldsymbol{r}_k|^2 \sin 2\phi_k}{\sum_{k=1}^{V} |\boldsymbol{r}_k|^2 \cos 2\phi_k}\right) \;, \tag{S4.16a}$$

$$\Delta\lambda = \sqrt{\left(\sum_{k=1}^{V} |\boldsymbol{r}_k|^2 \sin 2\phi_k\right)^2 + \left(\sum_{k=1}^{V} |\boldsymbol{r}_k|^2 \cos 2\phi_k\right)^2} \;, \tag{S4.16b}$$

where $\phi_k = \arctan(y_k/x_k)$ denotes the angular position of the $k-$th vertex with respect to the center of mass (Fig.4.1E). This construction implies that all components of the tensor $\boldsymbol{G}_2$ are proportional to either the real or imaginary part of the complex order parameter

$$\gamma_2 = \frac{1}{\Delta_2}\sum_{k=1}^{V} |\boldsymbol{r}_k|^2 e^{2i\phi_k} = \frac{\Delta\lambda}{\Delta_2}\,e^{2i\vartheta} \;, \tag{S4.17}$$

so that

$$|\gamma_2| = \frac{\Delta\lambda}{\Delta_2}\,, \qquad \vartheta = \frac{\operatorname{Arg}\gamma_2}{2}\,.$$

Now, the same construction can be carried out for a generic rank$-p$ shape tensor, by defining

$$\boldsymbol{G}_p = \frac{1}{\Delta_p}\left[\!\!\left[\sum_{k=1}^{V} \boldsymbol{r}_k^{\otimes p}\right]\!\!\right]\,, \tag{S4.18}$$

where $\Delta_p = \sum_{k=1}^{V} |\boldsymbol{r}_k|^p$. As for the rank$-2$ tensor defined in Eq.(S4.13), this tensor has only two linearly independent components, that are

$$g_1 = G_{p,xx\cdots x} = \frac{1}{2^{p-1}\Delta_p}\sum_{k=1}^{V} |\boldsymbol{r}_k|^p \cos\left(p\phi_k\right)\,, \tag{S4.19a}$$

$$g_2 = G_{p,xx\cdots y} = \frac{1}{2^{p-1}\Delta_p}\sum_{k=1}^{V} |\boldsymbol{r}_k|^p \sin\left(p\phi_k\right)\,, \tag{S4.19b}$$

and can be cast as in Eq.(S4.13), that is

$$\boldsymbol{G}_p = \frac{\Delta\lambda_p}{\Delta_p}\,[\![\boldsymbol{e}^{\otimes p}]\!]\,, \tag{S4.20}$$

where the positive scalar $\Delta\lambda_p$ and the unit vector $\boldsymbol{e} = \cos\vartheta_p\,\boldsymbol{e}_x + \sin\vartheta_p\,\boldsymbol{e}_y$ are analogous to the difference $\lambda_1 - \lambda_2$, quantifying the anisotropy of the polygon, and the eigenvector $\boldsymbol{e}_1$ associated with the largest eigenvalue. This problem ultimately relies on a generalization of the spectral theorem for tensors whose rank is larger than two. A possible strategy to achieve such as generalization was proposed by Virga in the context of rank-3 tensors (*15*) and consists of defining ϑ_p as the inclination of a $p-$legged star oriented in such a way to maximize the probability of finding a vertex of the polygon in the direction of either one of the legs. The latter task is equivalent to solving the system of equations

$$\boldsymbol{G}_p \odot \boldsymbol{e}^{\otimes p-1} = \frac{\Delta\lambda_p}{\Delta_p}\,\boldsymbol{e}\,, \tag{S4.21}$$

where $\odot$ denotes a contraction of all matching indices of the two tensors on the left-hand side. After some lengthy calculations, partially summarized in Sec. S4.4.1, one finds

$$\vartheta_p = \frac{1}{p}\arctan\left(\frac{\sum_{k=1}^{V}|\boldsymbol{r}_k|^p\sin(p\phi_k)}{\sum_{k=1}^{V}|\boldsymbol{r}_k|^p\cos(p\phi_k)}\right) , \tag{S4.22a}$$

$$\Delta\lambda_p = \sqrt{\left(\sum_{k=1}^{V}|\boldsymbol{r}_k|^p\cos(p\phi_k)\right)^2+\left(\sum_{k=1}^{V}|\boldsymbol{r}_k|^p\sin(p\phi_k)\right)^2} . \tag{S4.22b}$$

As in the case of the rank-2 shape tensor, one can then express all components of $\boldsymbol{G}_p$ in terms of the real and imaginary parts of the $p-$fold complex order parameter

$$\gamma_p = \frac{1}{\Delta_p}\sum_{k=1}^{V}|\boldsymbol{r}_k|^p e^{ip\phi_k} = \frac{\Delta\lambda_p}{\Delta_p}\, e^{ip\vartheta_p} , \tag{S4.23}$$

so that

$$|\gamma_p| = \frac{\Delta\lambda_p}{\Delta_p} , \qquad \vartheta = \frac{\operatorname{Arg}\gamma_p}{p} .$$

Derivation of Eqs.(S4.22)
For sake of completeness, here we elaborate on the solution of Eq.(S4.21), leading to Eqs.(S4.22). The strategy, pioneered in Ref. (*15*), consists of mapping the diagonalization of a rank$-p$ tensor to an optimization problem where $\Delta\lambda_p \in \mathbb{R}$ is the Lagrange multiplier subjected to the constraint $|\boldsymbol{e}|^2 = e_x^2+e_y^2 = 1$. This task requires computing the tensorial power $\boldsymbol{e}^{\otimes p-1}$, which, in turn, amounts to constructing all possible order$-(p-1)$ products of e_x and e_y. The latter is facilitated by the fact that, as previously stated, the two-dimensional tensor $\boldsymbol{G}_p$ has only two linearly independent components, proportional to the functions g_1 and g_2 introduced in Eqs.(S4.19). In particular, depending on whether the number of $y-$indices of the generic element $G_{i_1 i_2\cdots i_p}$, with $i_p = \{x, y\}$, is even or odd, the element is proportional to g_1 and g_2 respectively. Taken together, the aforementioned considerations result into the following expressions for the components of

the $\boldsymbol{e}$ vector:

$$\begin{aligned}\frac{\Delta\lambda_p}{\Delta_p}e_x &= g_1\left[\sum_{k\in\text{even}}(-1)^{\frac{k}{2}}\binom{p-1}{k}e_x^{p-1-k}e_y^k\right]\\ &+ g_2\left[\sum_{k\in\text{odd}}(-1)^{\frac{k-1}{2}}\binom{p-1}{k}e_x^{p-1-k}e_y^k\right], \qquad \text{(S4.24a)}\\ \frac{\Delta\lambda_p}{\Delta_p}e_y &= g_2\left[\sum_{k\in\text{even}}(-1)^{\frac{k}{2}}\binom{p-1}{k}e_x^{p-1-k}e_y^k\right]\\ &- g_1\left[\sum_{k\in\text{odd}}(-1)^{\frac{k-1}{2}}\binom{p-1}{k}e_x^{p-1-k}e_y^k\right]. \qquad \text{(S4.24b)}\end{aligned}$$

Despite their apparently complexity, these equations can be considerably simplified leading to

$$\frac{\Delta\lambda_p}{\Delta_p}\cos\vartheta_p = g_1\cos\left[(p-1)\,\vartheta_p\right] + g_2\sin\left[(p-1)\,\vartheta_p\right], \qquad \text{(S4.25a)}$$

$$\frac{\Delta\lambda_p}{\Delta_p}\sin\vartheta_p = g_2\cos\left[(p-1)\,\vartheta_p\right] - g_1\sin\left[(p-1)\,\vartheta_p\right]. \qquad \text{(S4.25b)}$$

If $g_1 = 0$, Eqs.(S4.25) reduces to

$$\cot\vartheta_p = \tan\left[(p-1)\,\vartheta_p\right]\ , \qquad \text{(S4.26)}$$

which has $2\,p$ solutions in the range $0 \leq \vartheta_p < 2\pi$ given by

$$\vartheta_p^{(k)} = \frac{2k+1}{p}\pi\ , \qquad k = 0,\, 1\ldots\, 2p-1\ . \qquad \text{(S4.27)}$$

Conversely, when $g_1 \neq 0$, setting $\varrho = g_2/g_1$ and solving Eqs.(S4.25) with respect to ϑ_p gives

$$\cot\vartheta_p = \frac{\cos\left[(p-1)\,\vartheta_p\right] + \varrho\sin\left[(p-1)\,\vartheta_p\right]}{\varrho\cos\left[(p-1)\,\vartheta_p\right] - \sin\left[(p-1)\,\vartheta_p\right]}\ , \qquad \text{(S4.28)}$$

from which one can readily find

$$\varrho = \tan p\vartheta_p\ , \qquad \text{(S4.29)}$$

whose solution is given by

$$\vartheta_p^{(k)} = \frac{\arctan\varrho + k\pi}{p}\ , \qquad k = 0,\, 1\ldots 2p-1\ , \qquad \text{(S4.30)}$$

thereby completing the derivation of Eq.(S4.22a). To compute $\Delta\lambda_p$, one can use again Eqs.(S4.25) and express g_1 and g_2 in terms of coordinates. This gives, after some direct calculations,

$$\begin{aligned}\left|\Delta\lambda_p^{(k)}\right| &= |g_1|\sqrt{1+\varrho^2}\\ &= \frac{1}{2^{p-1}}\sqrt{\left(\sum_{i=1}^{V}|\boldsymbol{r}_i|^p\cos\left(p\phi_i\right)\right)^2+\left(\sum_{i=1}^{V}|\boldsymbol{r}_i|^p\sin\left(p\phi_i\right)\right)^2}\ .\end{aligned} \tag{S4.31}$$

Note that, because of the periodicity of $\vartheta_p^{(k)}$, then $\Delta\lambda_p^{(k)} = -\lambda_p^{(k+1)}$, whereas the sign of $\lambda_p^{(0)}$ depends on ϱ and g_1. Finally, to cast the tensor $\boldsymbol{G}_p$ in the form given in Eq.(S4.20), one can write $g_1 = \Delta\lambda_p\hat{g}_1$ and $g_2 = \Delta\lambda_p\hat{g}_2$ where

$$\hat{g}_1 = \frac{1}{2^{p-1}\Delta_p}\cos p\vartheta_p\ , \qquad \hat{g}_2 = \frac{1}{2^{p-1}\Delta_p}\sin p\vartheta_p$$

are the two independent components of $[\![\boldsymbol{e}^{\otimes p}]\!]/\Delta_p$. Then, using the expression of ϑ_p given in Eq.(S4.27) and Eq.(S4.30), one obtains

$$\Delta\lambda_p = 2^{p-1}\left|\Delta\lambda_p^{(k)}\right|\ , \qquad k=0,1\dots 2p-1\ , \tag{S4.32}$$

which completes the derivation of Eq.(S4.22b).

S4.4.2 Defect representation in $p-$atic liquid crystals

In two-dimensional liquid crystals, topological defects consist of point-like singularities in the orientational field, that are points where the orientations of the director field are not univocally defined, and can be classified in terms of the winding number s defined in the main text. In liquid crystals with $p-$fold rotational symmetry, the latter is an integer multiple of the elementary winding number $1/p$. By contrast, it is impossible to correctly describe a defect of winding number $s = \pm\, 1/p$ in terms of an orientation field with rotational symmetry other than $p-$fold.

To substantiate this statement, we consider here the common case of a pair of $\pm\, 1/2$ disclinations in a nematic liquid crystal (p = 2), respectively located at positions $\boldsymbol{r}_+ = x_+\boldsymbol{e}_x + y_+\boldsymbol{e}_y$ and $\boldsymbol{r}_- = x_-\boldsymbol{e}_x + y_-\boldsymbol{e}_y$. The far-field configuration of the phase $\vartheta_2 = \mathrm{Arg}(\Gamma_2)/2$ is given by

$$\vartheta_2 = \frac{1}{2}\left[\arctan\left(\frac{y-y_+}{x-x_+}\right) - \arctan\left(\frac{y-y_-}{x-x_-}\right)\right]\ . \tag{S4.33}$$

In turn, the $2-$fold orientation field can be visualized as the standard headless nematic director – i.e. a $2-$legged star – as in Fig.4.1A of the main text. Now, as illustrated in Fig.4.3E, attempting to describe the same $2-$fold symmetric configuration with a, say, $1-$fold symmetric orientation filed – i.e. a standard vector field – results in a discontinuity of magnitude π of the associated phase ϑ_1 across the $x-$axis.

The same issue occurs while attempting to describe a pair of $s = \pm n/p$ defects (with n a real number) in by means of a $q-$fold orientation filed, with $q < p$. In this case, the far-field configuration of the phase ϑ_p is given by

$$\vartheta_p = \frac{n}{p}\left[\arctan\left(\frac{y-y_+}{x-x_+}\right) - \arctan\left(\frac{y-y_-}{x-x_-}\right)\right], \tag{S4.34}$$

and it can be graphically represented by a $p-$legged star oriented at angles $\vartheta_p + 2\pi n/p$, with $n = 1, 2 \ldots p$, so that the order parameter $\Gamma_p = |\Gamma_p| \exp(ip\vartheta_p)$ is continuous everywhere, but at the defect position. We attempt to describe the same configuration in terms of the order parameter $\Gamma_q = |\Gamma_q| \exp(iq\vartheta_q)$, corresponding to $q-$legged stars oriented at an angle $\vartheta_q + 2\pi n/q$, with $n = 1, 2 \ldots q < p$. For the purpose of this discussion, and without loss of generality, we set $y_+ = y_- = y_0$ and compute the variation of Γ_q. While crossing the line, the axis $y = y_0$ in the region comprised between the two defects ($x_- < x < x_+$). Since the $q-$legged star associated with the order parameter Γ_q is invariant under rotations by $2\pi/q$, the inclination of the leg closer to the $x-$axis undergoes a discontinuity of magnitude

$$|\Delta\vartheta_q| = 2\pi \min\left(\frac{n}{p}, \frac{|p-nq|}{pq}\right) . \tag{S4.35}$$

Thus, the field ϑ_q is continuous everywhere, but at the defect position ($|\Delta\vartheta_q| = 2\pi m/p$ with m any natural number) only when $p = q$ or nq is an integer multiple of p. In particular, describing a defect of winding number $s = 1/6$ ($n = 1$ and $p = 6$) by means of a nematic field with $q = 2$ would result into a jump of magnitude $|\Delta\vartheta_2| = \pi/3$ as shown in Fig.4.3E in the main text. The resulting configuration of the nematic director features a singular line connecting defects of opposite charge.

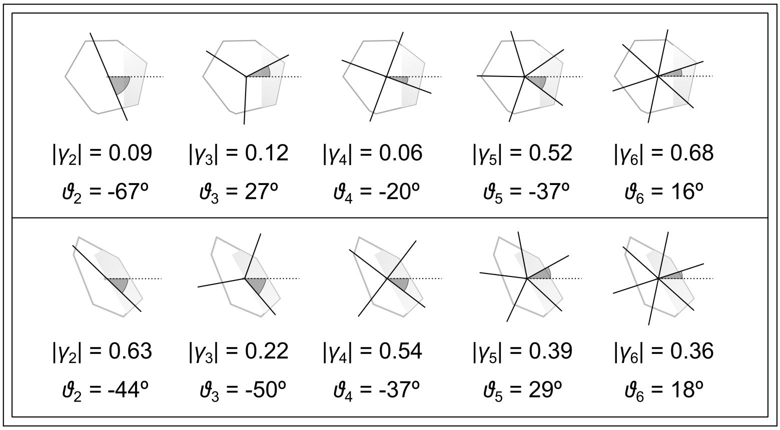

Figure S4.4: Order parameter γ_p***.*** *Top and bottom panels show the* $p-$*atic star for the polygonal shapes in Fig.4.1E and Fig.4.1F, respectively. The magnitude of the order parameter* $|\gamma_p|$ *and its orientation* ϑ_p *with respect to the polar axis (dashed horizontal line) are given for* $p = 2, \ldots, 6$*.*

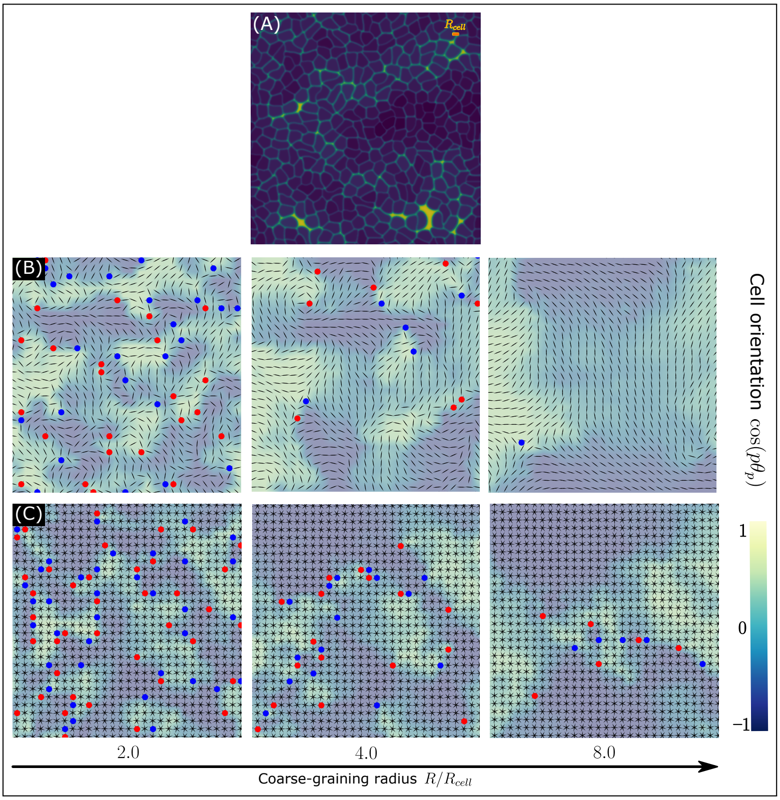

Figure S4.5: Coarse-graining the multiphase field model. *(**A**), A typical configuration of the multiphase field simulations with 360 cells. Darker regions correspond to areas dense with cells and lighter regions to areas where cells are sparser. (**B,C**), Nematic (top row) and hexatic (bottom row) coarse-grained fields* Γ_2 *and* Γ_6 *versus the coarse-graining radius* R*, expressed in units of the nominal cell size* R_{cell}*. In both panels, positive and negative defects are marked in red and blue respectively (*$\pm 1/2$ *for nematic and* $\pm 1/6$ *for hexatic).*

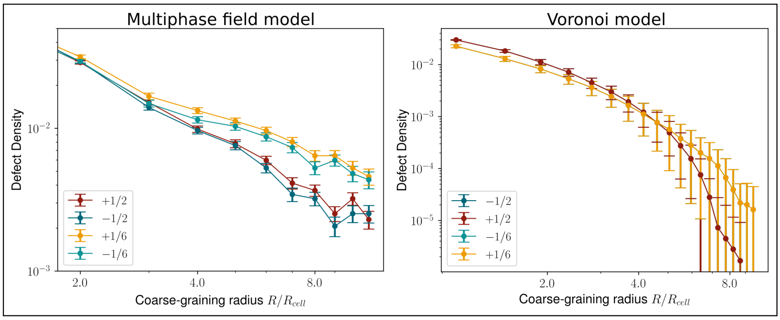

Figure S4.6: Decay of defect density in simulations. *Left and right panels show the decay of the defect density at varying the coarse-graining radius in simulations of the multiphase field model (left) and Voronoi model (right). The scaling of multiphase field model data is compatible with that shown in Fig.4.3D in the main text for experimental data. In the right panel, curves of oppositely charged defects overlap exactly.*

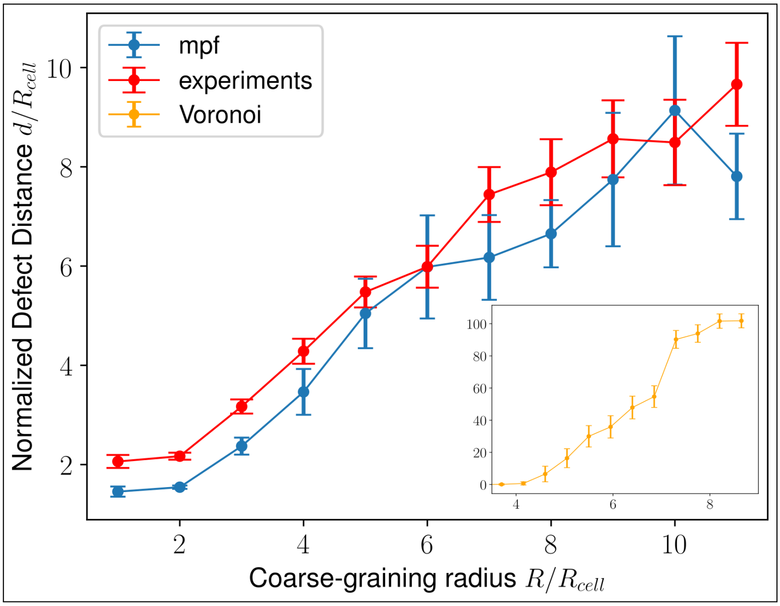

Figure S4.7: Separation of hexatic and nematic defects at varying the coarse-graining radius. *The graph shows the mean distance between a hexatic defect and the closest nematic defect, regardless of their charge, computed for experimental data, multiphase field simulations and Voronoi simulations (inset). Experimental data (red curve) and multiphase field simulation (blue curve) are in qualitative agreement.*

References

(*1*) Duclos, G., Erlenkämper, C., Joanny, J.-F., and Silberzan, P. (2016). Topological defects in confined populations of spindle-shaped cells. *Nat. Phys. 13*, 58–62.

(*2*) Saw, T. B., Doostmohammadi, A., Nier, V., Kocgozlu, L., Thampi, S., Toyama, Y., Marcq, P., Lim, C. T., Yeomans, J. M., and Ladoux, B. (2017). Topological defects in epithelia govern cell death and extrusion. *Nature 544*, 212–216.

(*3*) Kawaguchi, K., Kageyama, R., and Sano, M. (2017). Topological defects control collective dynamics in neural progenitor cell cultures. *Nature 545*, 327–331.

(*4*) Balasubramaniam, L., Doostmohammadi, A., Saw, T. B., Narayana, G. H. N. S., Mueller, R., Dang, T., Thomas, M., Gupta, S., Sonam, S., Yap, A. S., Toyama, Y., Mège, R.-M., Yeomans, J. M., and Ladoux, B. (2021). Investigating the nature of active forces in tissues reveals how contractile cells can form extensile monolayers. *Nature Materials 20*, 1156–1166.

(*5*) Li, Y.-W., and Ciamarra, M. P. (2018). Role of cell deformability in the two-dimensional melting of biological tissues. *Phys. Rev. Materials 2*, 045602.

(*6*) Durand, M., and Heu, J. (2019). Thermally driven order-disorder transition in two-dimensional soft cellular systems. *Phys. Rev. Lett. 123*, 188001.

(*7*) Pasupalak, A., Yan-Wei, L., Ni, R., and Pica Ciamarra, M. (2020). Hexatic phase in a model of active biological tissues. *Soft Matter 16*, 3914–3920.

(*8*) Maroudas-Sacks, Y., Garion, L., Shani-Zerbib, L., Livshits, A., Braun, E., and Keren, K. (2021). Topological defects in the nematic order of actin fibres as organization centres of Hydra morphogenesis. *Nature Physics 17*, 251–259.

(*9*) Hoffmann, L. A., Carenza, L. N., Eckert, J., and Giomi, L. (2022). Theory of defect-mediated morphogenesis. *Science Advances 8*, eabk2712.

(*10*) Streichan, S. J., Lefebvre, M. F., Noll, N., Wieschaus, E. F., and Shraiman, B. I. (2018). Global morphogenetic flow is accurately predicted by the spatial distribution of myosin motors. *Elife 7*, e27454.

(*11*) Bigun, J., *Optimal orientation detection of linear symmetry*; Linköping University Electronic Press: 1987.

(*12*) Aubouy, M., Jiang, Y., Glazier, J. A., and Graner, F. (2003). A texture tensor to quantify deformations. *Granul. Matter 5*, 67–70.

(*13*) Asipauskas, M., Aubouy, M., Glazier, J. A., Graner, F., and Jiang, Y. (2003). A texture tensor to quantify deformations: the example of two-dimensional flowing foams. *Granul. Matter 5*, 71–74.

(*14*) Chaikin, P. M., and Lubensky, T. C., *Principles of condensed matter physics*; Cambridge University Press: Cambridge, 1995.

(*15*) Friedel, G. (1922). Les états mésomorphes de la matière. *Ann. Phys. 9*, 273–474.

(*16*) Giomi, L., Toner, J., and Sarkar, N. (2022). Long-Ranged Order and Flow Alignment in Sheared $p-$atic Liquid Crystals. *Phys. Rev. Lett. 129*, 067801.

(*17*) Giomi, L., Toner, J., and Sarkar, N. (2022). Hydrodynamic theory of p-atic liquid crystals. *Phys. Rev. E 106*, 024701.

(*18*) Virga, E. G. (2015). Octupolar order in two dimensions. *Eur. Phys. J. E 38*, 63.

(*19*) Loewe, B., Chiang, M., Marenduzzo, D., and Marchetti, M. C. (2020). Solid-liquid transition of deformable and overlapping active particles. *Phys. Rev. Lett. 125*, 038003.

(*20*) Monfared, S., Ravichandran, G., Andrade, J. E., and Doostmohammadi, A. (2021). Mechanics of live cell elimination. *arXiv:2108.07657.*

(*21*) Carenza, L. N., Gonnella, G., Lamura, A., Negro, G., and Tiribocchi, A. (2019). Lattice Boltzmann methods and active fluids. *Eur. Phys. J. E 42*, 81.

(*22*) Bi, D., Yang, X., Marchetti, M. C., and Manning, M. L. (2016). Motility-driven glass and jamming transitions in biological tissues. *Physical review. X 6*, 021011.

(*23*) Kittel, C., and McEuen, P., *Introduction to solid state physics*; Wiley New York: 1996; Vol. 8.

(*24*) De Pascalis, C., and Etienne-Manneville, S. (2017). Single and collective cell migration: the mechanics of adhesions. *Mol. Biol. Cell 28*, 1833–1846.

(*25*) Friedl, P., and Gilmour, D. (2009). Collective cell migration in morphogenesis, regeneration and cancer. *Nat. Rev. Mol. Cell Bio. 10*, 445–457.

(*26*) Keber, F. C., Loiseau, E., Sanchez, T., DeCamp, S. J., Giomi, L., Bowick, M. J., Marchetti, M. C., Dogic, Z., and Bausch, A. R. (2014). Topology and dynamics of active nematic vesicles. *Science 345*, 1135–1139.

(*27*) Guillamat, P., Blanch-Mercader, C., Pernollet, G., Kruse, K., and Roux, A. (2022). Integer topological defects organize stresses driving tissue morphogenesis. *Nature Materials 21*, 588–597.

(*28*) Armengol-Collado, J.-M., Carenza, L. N., and Giomi, L. (2022). Hydrodynamics and multiscale order in confluent epithelia. *arXiv:2202.00651.*

(*29*) Blankenship, J. T., Backovic, S. T., Sanny, J. S., Weitz, O., and Zallen, J. A. (2006). Multicellular Rosette Formation Links Planar Cell Polarity to Tissue Morphogenesis. *Dev. Cell 11*, 459–470.

(*30*) Rauzi, M. (2020). Cell intercalation in a simple epithelium. *Phil. Trans. R. Soc. B 375*, 20190552.

(*31*) Haeger, A., Alexander, S., Vullings, M., Kaiser, F. M., Veelken, C., Flucke, U., Koehl, G. E., Hirschberg, M., Flentje, M., Hoffman, R. M., et al. (2020). Collective cancer invasion forms an integrin-dependent radioresistant niche. *J. Exp. Med> 217.*

(*32*) Serra-Picamal, X., Conte, V., Vincent, R., Anon, E., Tambe, D. T., Bazellieres, E., Butler, J. P., Fredberg, J. J., and Trepat, X. (2012). Mechanical waves during tissue expansion. *Nat. Phys. 8*, 628–634.

(*33*) Yamada, S., Pokutta, S., Drees, F., Weis, W. I., and Nelson, W. J. (2005). Deconstructing the Cadherin-Catenin-Actin Complex. *Cell 123*, 889–901.

(*34*) Maroudas-Sacks, Y., Garion, L., Shani-Zerbib, L., Livshits, A., Braun, E., and Keren, K. (2021). Topological defects in the nematic order of actin fibres as organization centres of Hydra morphogenesis. *Nature Physics 17*, 251–259.